Polarization-sensitive optical frequency domain imaging based on unpolarized light

Ki Hean Kim[1], B. Hyle Park[2], Yupeng Tu[3], Tayyaba Hasan[3], Byunghak Lee[1], Jianan Li[4], and Johannes F. de Boer[3, 4,*]

[1] *Dept. of Mechanical Engineering and Division of Integrative Biosciences and Biotechnology, Pohang University of Science and Technology, Pohang 790-784, Korea*
[2] *Dept. of Bioengineering, UC Riverside, Riverside, CA 92521, USA*
[3] *Wellman Center for Photomedicine, Massachusetts General Hospital, Boston, MA 02114, USA*
[4] *Institute for Lasers, Life and Biophotonics Amsterdam, Department of Physics and Astronomy, VU University, de Boelelaan 1081, 1081 HV Amsterdam, Netherlands*
*jfdeboer@few.vu.nl

Abstract: Polarization-sensitive optical coherence tomography (PS-OCT) is an augmented form of OCT, providing 3D images of both tissue structure and polarization properties. We developed a new method of polarization-sensitive optical frequency domain imaging (PS-OFDI), which is based on a wavelength-swept source. In this method the sample was illuminated with unpolarized light, which was composed of two orthogonal polarization states (i.e., separated by 180° in the Poincaré sphere) that are uncorrelated to each other. Reflection of these polarization states from within the sample was detected simultaneously and independently using a frequency multiplexing scheme. This simultaneous sample probing with two polarization states enabled determination of the depth-resolved Jones matrices of the sample. Polarization properties of the sample were obtained by analyzing the sample Jones matrices through eigenvector decomposition. The new PS-OFDI system ran at 31K wavelength-scans/s with 3072 pixels per wavelength-scan, and was tested by imaging a polarizer and several birefringent tissues such as chicken muscle and human skin. Lastly the new PS-OFDI was applied to imaging two cancer animal models: a mouse model by injecting cancer cells and a hamster cheek pouch model. These animal model studies demonstrated the significant differences in tissue polarization properties between cancer and normal tissues in vivo.

©2011 Optical Society of America

OCIS codes: (170.4500) optical coherence tomography; (170.3880) medical and biological imaging; (260.5430) polarization; (260.1440) birefringence; (110.4500) optical coherence tomography.

References and links

1. J. F. de Boer, T. E. Milner, M. J. C. van Gemert, and J. S. Nelson, "Two-dimensional birefringence imaging in biological tissue by polarization-sensitive optical coherence tomography," Opt. Lett. **22**(12), 934–936 (1997), http://www.opticsinfobase.org/abstract.cfm?URI=ol-22-12-934.
2. J. F. de Boer, and T. E. Milner, "Review of polarization sensitive optical coherence tomography and Stokes vector determination," J. Biomed. Opt. **7**(3), 359–371 (2002).
3. D. Huang, E. A. Swanson, C. P. Lin, J. S. Schuman, W. G. Stinson, W. Chang, M. R. Hee, T. Flotte, K. Gregory, C. A. Puliafito, and J. G. Fujimoto, "Optical coherence tomography," Science **254**(5035), 1178–1181 (1991).
4. B. Cense, T. C. Chen, B. H. Park, M. C. Pierce, and J. F. de Boer, "Thickness and birefringence of healthy retinal nerve fiber layer tissue measured with polarization-sensitive optical coherence tomography," Invest. Ophthalmol. Vis. Sci. **45**(8), 2606–2612 (2004).
5. M. Pircher, E. Götzinger, O. Findl, S. Michels, W. Geitzenauer, C. Leydolt, U. Schmidt-Erfurth, and C. K. Hitzenberger, "Human macula investigated in vivo with polarization-sensitive optical coherence tomography," Invest. Ophthalmol. Vis. Sci. **47**(12), 5487–5494 (2006).
6. M. Miura, M. Yamanari, T. Iwasaki, A. E. Elsner, S. Makita, T. Yatagai, and Y. Yasuno, "Imaging polarimetry in age-related macular degeneration," Invest. Ophthalmol. Vis. Sci. **49**(6), 2661–2667 (2008).
7. M. Yamanari, M. Miura, S. Makita, T. Yatagai, and Y. Yasuno, "Phase retardation measurement of retinal nerve fiber layer by polarization-sensitive spectral-domain optical coherence tomography and scanning laser polarimetry," J. Biomed. Opt. **13**(1), 014013 (2008).

8. C. Ahlers, E. Götzinger, M. Pircher, I. Golbaz, F. Prager, C. Schütze, B. Baumann, C. K. Hitzenberger, and U. Schmidt-Erfurth, "Imaging of the retinal pigment epithelium in age-related macular degeneration using polarization-sensitive optical coherence tomography," Invest. Ophthalmol. Vis. Sci. **51**(4), 2149–2157 (2010).
9. B. H. Park, C. Saxer, S. M. Srinivas, J. S. Nelson, and J. F. de Boer, "In vivo burn depth determination by high-speed fiber-based polarization sensitive optical coherence tomography," J. Biomed. Opt. **6**(4), 474–479 (2001).
10. J. Strasswimmer, M. C. Pierce, B. H. Park, V. Neel, and J. F. de Boer, "Polarization-sensitive optical coherence tomography of invasive basal cell carcinoma," J. Biomed. Opt. **9**(2), 292–298 (2004).
11. M. C. Pierce, R. L. Sheridan, B. Hyle Park, B. Cense, and J. F. de Boer, "Collagen denaturation can be quantified in burned human skin using polarization-sensitive optical coherence tomography," Burns **30**(6), 511–517 (2004).
12. M. C. Pierce, J. Strasswimmer, B. H. Park, B. Cense, and J. F. de Boer, "Advances in optical coherence tomography imaging for dermatology," J. Invest. Dermatol. **123**(3), 458–463 (2004).
13. S. K. Nadkarni, M. C. Pierce, B. H. Park, J. F. de Boer, P. Whittaker, B. E. Bouma, J. E. Bressner, E. Halpern, S. L. Houser, and G. J. Tearney, "Measurement of collagen and smooth muscle cell content in atherosclerotic plaques using polarization-sensitive optical coherence tomography," J. Am. Coll. Cardiol. **49**(13), 1474–1481 (2007).
14. J. A. Burns, S. M. Zeitels, R. R. Anderson, J. B. Kobler, M. C. Pierce, and J. F. de Boer, "Imaging the mucosa of the human vocal fold with optical coherence tomography," Ann. Otol. Rhinol. Laryngol. **114**(9), 671–676 (2005).
15. K. H. Kim, J. A. Burns, J. J. Bernstein, G. N. Maguluri, B. H. Park, and J. F. de Boer, "In vivo 3D human vocal fold imaging with polarization sensitive optical coherence tomography and a MEMS scanning catheter," Opt. Express **18**(14), 14644–14653 (2010), http://www.opticsinfobase.org/abstract.cfm?URI=oe-18-14-14644.
16. M. R. Hee, D. Huang, E. A. Swanson, and J. G. Fujimoto, "Polarization-sensitive low-coherence reflectometer for birefringence characterization and ranging," J. Opt. Soc. Am. B **9**(6), 903–908 (1992).
17. J. F. de Boer, T. E. Milner, and J. S. Nelson, "Determination of the depth-resolved Stokes parameters of light backscattered from turbid media by use of polarization-sensitive optical coherence tomography," Opt. Lett. **24**(5), 300–302 (1999), http://www.opticsinfobase.org/ol/abstract.cfm?URI=ol-24-5-300.
18. G. Yao, and L. V. Wang, "Two-dimensional depth-resolved Mueller matrix characterization of biological tissue by optical coherence tomography," Opt. Lett. **24**(8), 537–539 (1999), http://www.opticsinfobase.org/abstract.cfm?URI=ol-24-8-537.
19. C. E. Saxer, J. F. de Boer, B. H. Park, Y. Zhao, Z. Chen, and J. S. Nelson, "High-speed fiber based polarization-sensitive optical coherence tomography of in vivo human skin," Opt. Lett. **25**(18), 1355–1357 (2000), http://www.opticsinfobase.org/abstract.cfm?URI=ol-25-18-1355.
20. J. E. Roth, J. A. Kozak, S. Yazdanfar, A. M. Rollins, and J. A. Izatt, "Simplified method for polarization-sensitive optical coherence tomography," Opt. Lett. **26**(14), 1069–1071 (2001), http://www.opticsinfobase.org/ol/abstract.cfm?URI=ol-26-14-1069.
21. C. K. Hitzenberger, E. Goetzinger, M. Sticker, M. Pircher, and A. F. Fercher, "Measurement and imaging of birefringence and optic axis orientation by phase resolved polarization sensitive optical coherence tomography," Opt. Express **9**(13), 780–790 (2001), http://www.opticsinfobase.org/abstract.cfm?URI=oe-9-13-780.
22. S. L. Jiao, and L. V. Wang, "Two-dimensional depth-resolved Mueller matrix of biological tissue measured with double-beam polarization-sensitive optical coherence tomography," Opt. Lett. **27**(2), 101–103 (2002), http://www.opticsinfobase.org/abstract.cfm?URI=ol-27-2-101.
23. S. Jiao, W. Yu, G. Stoica, and L. V. Wang, "Optical-fiber-based Mueller optical coherence tomography," Opt. Lett. **28**(14), 1206–1208 (2003), http://www.opticsinfobase.org/ol/abstract.cfm?URI=ol-28-14-1206.
24. J. Zhang, W. Jung, J. Nelson, and Z. Chen, "Full range polarization-sensitive Fourier domain optical coherence tomography," Opt. Express **12**(24), 6033–6039 (2004), http://www.opticsinfobase.org/oe/abstract.cfm?URI=oe-12-24-6033.
25. E. Götzinger, M. Pircher, and C. K. Hitzenberger, "High speed spectral domain polarization sensitive optical coherence tomography of the human retina," Opt. Express **13**(25), 10217–10229 (2005), http://www.opticsinfobase.org/oe/abstract.cfm?URI=oe-13-25-10217.
26. B. H. Park, M. C. Pierce, B. Cense, S. H. Yun, M. Mujat, G. J. Tearney, B. E. Bouma, and J. F. de Boer, "Real-time fiber-based multi-functional spectral-domain optical coherence tomography at 1.3 μm," Opt. Express **13**(11), 3931–3944 (2005), http://www.opticsinfobase.org/abstract.cfm?URI=oe-13-11-3931.
27. W. Y. Oh, S. H. Yun, B. J. Vakoc, M. Shishkov, A. E. Desjardins, B. H. Park, J. F. de Boer, G. J. Tearney, and B. E. Bouma, "High-speed polarization sensitive optical frequency domain imaging with frequency multiplexing," Opt. Express **16**(2), 1096–1103 (2008), http://www.opticsinfobase.org/oe/abstract.cfm?URI=oe-16-2-1096.
28. M. Yamanari, S. Makita, and Y. Yasuno, "Polarization-sensitive swept-source optical coherence tomography with continuous source polarization modulation," Opt. Express **16**(8), 5892–5906 (2008), http://www.opticsinfobase.org/abstract.cfm?URI=oe-16-8-5892.
29. W. Y. Oh, B. J. Vakoc, S. H. Yun, G. J. Tearney, and B. E. Bouma, "Single-detector polarization-sensitive optical frequency domain imaging using high-speed intra A-line polarization modulation," Opt. Lett. **33**(12), 1330–1332 (2008), http://www.opticsinfobase.org/abstract.cfm?URI=ol-33-12-1330.
30. E. Götzinger, B. Baumann, M. Pircher, and C. K. Hitzenberger, "Polarization maintaining fiber based ultra-high resolution spectral domain polarization sensitive optical coherence tomography," Opt. Express **17**(25), 22704–22717 (2009), http://www.opticsinfobase.org/oe/abstract.cfm?URI=oe-17-25-22704.
31. M. K. Al-Qaisi, and T. Akkin, "Swept-source polarization-sensitive optical coherence tomography based on polarization-maintaining fiber," Opt. Express **18**(4), 3392–3403 (2010), http://www.opticsinfobase.org/oe/abstract.cfm?URI=oe-18-4-3392.

32. S. H. Yun, G. J. Tearney, J. F. de Boer, and B. E. Bouma, "Removing the depth-degeneracy in optical frequency domain imaging with frequency shifting," Opt. Express **12**(20), 4822–4828 (2004), http://www.opticsinfobase.org/abstract.cfm?URI=oe-12-20-4822.
33. B. H. Park, M. C. Pierce, B. Cense, and J. F. de Boer, "Jones matrix analysis for a polarization-sensitive optical coherence tomography system using fiber-optic components," Opt. Lett. **29**(21), 2512–2514 (2004), http://www.opticsinfobase.org/abstract.cfm?URI=ol-29-21-2512.
34. R. A. Chipman, "Polarization analysis of optical systems," Opt. Eng. **28**, 90-91 (1989).
35. J. J. Salley, "Experimental carcinogenesis in the cheek pouch of the Syrian hamster," J. Dent. Res. **33**(2), 253–262 (1954).
36. J. J. Gil, and E. Bernabeu, "Obtainment of the polarizing and retardation parameters of a non-depolarizing optical system from the polar decomposition of its Mueller matrix," Optik (Stuttg.) **76**, 67–71 (1987).

1. Introduction

Polarization-sensitive optical coherence tomography (PS-OCT) is an augmented form of OCT [1,2]. OCT is a 3D imaging technique based on light back-reflected from within tissues [3]. While OCT provides structural information of tissues, PS-OCT provides additional information of tissue polarization properties simultaneously with structure by detecting depth resolved polarization state changes of reflected light. Biological tissues have various polarization properties such as birefringence, diattenuation, and depolarization. Tissue birefringence is originated from either organized microstructures or collagen composition [2]. There are various birefringent tissues, e.g. muscle, tendon, cartilage, dermis of skin, coronary artery, anterior eye segment, retinal nerve fiber layer, and vocal fold. The potential of PS-OCT has been demonstrated in pre-clinical and clinical studies of various organs such as the eye [4–8], skin [9–12], coronary artery [13], and vocal fold [14,15].

There have been various PS-OCT methods developed [1,16–31]. PS-OCT measures sample polarization properties by detecting depth-resolved polarization state changes of reflected light with respect to the incident polarization. Although the amount of polarization change varies depending on the incident polarization state and sample orientation (optic axis), several PS-OCT methods have been developed to reliably determine sample polarization properties. In a bulk-optic setup, circular polarization was used as the incident polarization state to detect linear birefringence of the sample [16,17]. Various optical fiber based methods have been developed for flexible assessment of internal and external organs [18–20,22–24,26,27]. Unlike bulk-optic based methods, fiber based methods do not have control over the incident polarization state(s) onto the sample, due to the birefringence of optical fibers in the sample arm of an interferometer setup. Therefore, these methods used at least two different incident polarization states for sample probing. One method alternated source polarization states in every depth-scan by using a polarization modulator, such that adjacent depth-scans were acquired with different incident polarization states [19]. Sample polarization properties were calculated by combining information of two adjacent depth-scans. This method had a restriction in lateral scanning speed: since two depth-scans with different incident polarization states should be in principle acquired at (nearly) the same position, the speed of lateral scanning was limited to ensure enough overlap between adjacent wavelength-scans [26]. Recently several PS-OCT methods capable of measuring polarization properties within a single wavelength-scan were developed to overcome this limitation [27–29]. These methods used two incident polarization states in single wavelength-scans. One method combined two polarization states into one by encoding them at different carrier frequencies, and sample reflections were separated by frequency demodulation, and is referred as frequency multiplexing [27]. Other methods were based on modulation of the source polarization state at speeds much higher than that of the wavelength-scan. One method modulated the source polarization state at one quarter of the data acquisition frequency such that four polarization states alternated to measure the Stokes vector components within single wavelength-scans [29]. The other method modulated the source polarization state at two thirds of the data acquisition frequency, generating two different polarization states and frequency shifting within single wavelength-scans [28].

We developed a new PS-OCT method by extending the first single wavelength-scan method based on frequency multiplexing. This previous method used two different

polarization states separated by 90° in the Poincaré sphere for sample probing. This polarization state combination ensures the reliable measurement of sample's polarization properties: even if one of two incident polarization states is aligned with the optic axis of a birefringent tissue and thus its reflected polarization does not change, the other incident polarization state will incur a maximal change of the polarization state in its reflection. This method was originally developed for the PS-OCT method, which measured two adjacent depth-scans sequentially with alternating incident polarization states [19]. Since this single wavelength-scan method probes with two polarization states simultaneously, a phase relationship between two reflected polarization states is available. This phase relationship can be used to calculate sample's polarization properties, and the previous restriction on the choice of polarization combination, which was 90° separation in the Poincaré sphere, is no longer required. Therefore, this new method utilized the phase relationship of two reflected polarization states. This method probed a sample with unpolarized light, which was a combination of two uncorrelated polarization states separated by 180° on the Poincaré sphere. Reflected polarization states from the sample were measured by using a frequency multiplexing scheme. In this manuscript, we will describe the system design and implementation, polarization analysis method, and various imaging results including both ex-vivo and in-vivo birefringent tissues, and in-vivo animal cancer models.

2. Material and methods

2.1. System configuration

The schematic of the new system is shown in Fig. 1. Its light source was a wavelength-swept source based on a polygon-scanner filter. The repetition rate of the source was 31K wavelength-scans/s with an output of 40 mW, a bandwidth of 120 nm centered at 1295 nm, and a spectral line width of 0.23 nm corresponding to a one sided depth range of 1.6 mm in air. A small portion (10%) of light from the source was tapped to the combination of a circulator (AC photonics, CA) and a fiber Bragg grating (FBG, OE-land, Canada) to generate a trigger signal for each sweep of the source, and the rest (90%) was used for imaging. Light from the source first passed through an unpolarizer. Input light of the unpolarizer was linearly polarized at 45° with the horizontal axis by using a linear polarizer after a polarization controller, and then was split into horizontal and vertical polarization states in equal amounts by a polarizing beam splitter (PBS). These two polarization states were decorrelated with respect to each other by introducing a relative delay of 9 cm, and were recombined by using another PBS. Then, output light was completely unpolarized.

After the unpolarizer, 90% of the power was directed to the sample arm of an interferometer setup for sample probing, and the remaining 10% was directed to the transmission reference arm. In the reference arm, unpolarized light was split into two orthogonal polarization states by using a PBS. A polarization controller between the unpolarizer and reference arm was adjusted such that the same two linear polarization states, which were generated in the unpolarizer, were generated again in the reference arm.
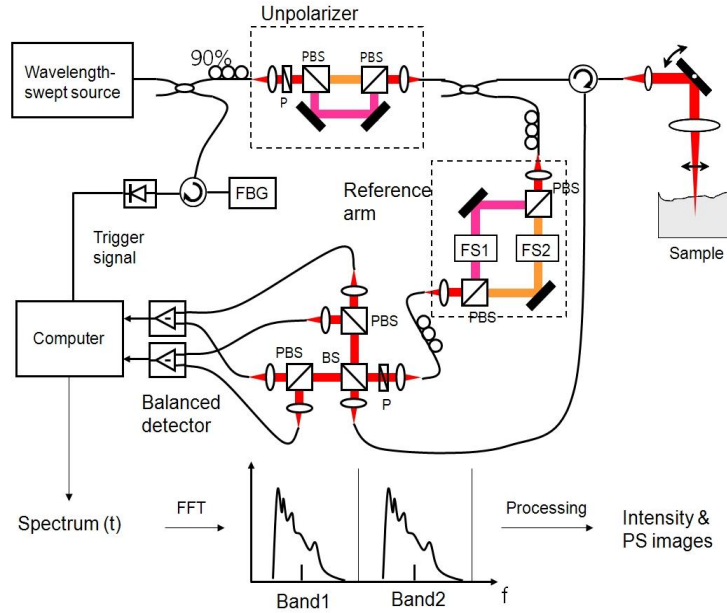
Fig. 1. Schematic of PS-OFDI based on unpolarized light. PBS: polarizing beam splitter, P: polarizer, BS: beam splitter, FS: frequency shifter, FBG: fiber Bragg grating

This polarization control was not necessary for the principle of the functionality, but was used in order to minimize a high Relative Intensity Noise (RIN) which will be discussed later. These two polarization states were frequency shifted at 20 MHz and 40 MHz respectively by a pair of acousto-optic modulators (Brimrose Inc, NC) for the frequency multiplexing scheme. These AOMs were driven by a single reference clock for synchronization. This frequency shifting was also advantageous in doubling the imaging depth range to 3.2 mm in air [32]. After the AOM's, the two orthogonal polarization states were recombined by a PBS and coupled into a single-mode fiber. Light from the reference transmission arm was combined with reflected light from the sample for interference in a detection arm, and the interference signal was detected by a polarization-diverse balanced detection setup. In the detection arm, light from the reference arm first passed through a polarization controller, and then a polarizer oriented at 45° with respect to the horizontal axis. This combination of the polarization controller and polarizer ensured that each polarization state, which was frequency shifted in the reference arm, was detected by each channel of the balanced receivers with equal intensity. Signals from the two balanced receivers were acquired simultaneously by an ADC board (PDA14, Signatec Inc, CA) running at 100 MHz sampling frequency. Out of the available signal bandwidth of 50 MHz, signals of individual polarization states occupied separate detection bands: one from 10MHz to 30MHz, and the other from 30MHz to 50MHz. Synchronization between actuators (galvo's for scanning the sample arm beam) and ADC board was configured by using a field programmable logic array (FPGA) demo board (Spartan3, Digilent). The FPGA board used the 100MHz sampling clock from the ADC board as a reference clock, and generated triggering and driving signals based on the reference clock.

The acquired spectra were Fourier transformed into the frequency domain, and then individual frequency bands were demodulated. The demodulated spectra were inverse Fourier transformed to the time domain. Then, the time to k-space mapping was applied by using pre-calibrated wavelength data and interpolation. Dispersion compensation was applied to the spectra by using a pre-calibration of the dispersion mismatch between reference and sample arms. Finally the spectra in equal k-space were Fourier transformed into reflectivity profiles in depth (z) space. The measured sensitivity was 98 dB, about 17 dB lower compared with the

theoretical sensitivity of 115dB, and 7-8 dB lower compared to other published OCT systems. We observed that the RIN of the source increased significantly after the unpolarizer, when a linear polarizer was placed at an orientation of 45° with the horizontal axis. This indicated that despite a 9 cm delay, there still was coherence between the orthogonal polarization states. We attributed this coherence to the narrow line width associated with the cavity mode spacing of the laser (100 MHz). The polarizer or the PBS's in the detection unit acted as the polarizer in this measurement setup. The additional 7-8 dB of noise was due to incomplete suppression by the balanced detection of this RIN, and light intensity fluctuations generated by the frequency shifters. Intensity images were obtained by adding up intensities of both channels and bands, and polarization-sensitive (PS) images were generated by analyzing the obtained complex depth profiles in the procedure described in the next paragraph.

2.2. PS analysis method

The PS analysis method for this new PS-OFDI was based on a previous Jones matrix analysis method [33]. This analysis method was originally developed for the PS-OCT which measured two adjacent wavelength-scans with alternating source polarization states. The non-unpolarizing polarization properties of an optical system can be completely described by its complex Jones matrix $\mathbf{J}$, which transforms an incident polarization, described by a complex electric field vector $\mathbf{E} = [H\ V]^T$, to a transmitted polarization $\mathbf{E}' = [H'\ V']^T$ as $\mathbf{E}' = \mathbf{J}\,\mathbf{E}$. An equation for the sample Jones matrix could be constructed by combining two Jones matrix equations with individual incident polarization states. Assuming that the reflected polarization states from the sample were represented as $\left[H_1'\ V_1'\right]^T$, $\left[H_2'\ V_2'\right]^T$ at the depth z, and as $\left[H_1\ V_1\right]^T$, $\left[H_2\ V_2\right]^T$ on the surface (z = 0) respectively with subscripts 1 and 2 indicating two different polarization states, the Jones matrix equation transforming these surface polarization states to the polarization states at the depth was formulated as

$$\begin{bmatrix} H_1' & H_2' \\ V_1' & V_2' \end{bmatrix} = \mathbf{J}_{\text{out}}\mathbf{J}_S\mathbf{J}_{\text{out}}^{-1}\begin{bmatrix} H_1 & H_2 \\ V_1 & V_2 \end{bmatrix},$$

where $\mathbf{J}_{\text{out}}$ represented the optical path from the sample surface to detectors, and $\mathbf{J}_s$ the round-trip Jones matrix of the sample. Then, $\mathbf{J}_{\text{out}}\mathbf{J}_S\mathbf{J}_{\text{out}}^{-1}$ represented the round trip of the output path and sample. This equation had a very similar but simpler shape than the previous Jones matrix analysis method, because the two measurements were simultaneous and there was no phase ambiguity between them. In our previous work, measurements with different polarization states were sequential, which introduced an additional phase factor [33]. By simplifying $\mathbf{J}_{\text{out}}\mathbf{J}_S\mathbf{J}_{\text{out}}^{-1}$ as the sample equivalent matrix $\mathbf{J}_T$, the above equation becomes,

$$\mathbf{J}_T = \begin{bmatrix} H_1' & H_2' \\ V_1' & V_2' \end{bmatrix}\begin{bmatrix} H_1 & H_2 \\ V_1 & V_2 \end{bmatrix}^{-1}.$$

This equation shows that $\mathbf{J}_T$ can be obtained directly from the measurement.

Polarization properties of the sample were obtained by analyzing $\mathbf{J}_T$. We adopted a simple analysis method: it was assumed that the sample shares the same optic axes for birefringence and diattenuation. Then, $\mathbf{J}_T$ could be decomposed into the format of $\mathbf{J}_T = \mathbf{U}\,\mathbf{D}\,\mathbf{U}^{-1}$, where $\mathbf{U}$ is a unitary matrix representing the orientation of the optic axis and $\mathbf{D}$ is a diagonal matrix whose diagonal elements contain the polarization parameters. The assumption about the optic axes was also adopted in previous PS analysis methods [23,33]. We decomposed $\mathbf{J}_T$ by using eigenvector decomposition: $\mathbf{J}_T = \mathbf{V}\boldsymbol{\Lambda}\mathbf{V}^{-1}$ where $\boldsymbol{\Lambda}$ was a diagonal matrix, and $\mathbf{V}$ was a matrix composed of two eigenvectors as column vectors. The components of the diagonal matrix $\boldsymbol{\Lambda}$

were $p_1 e^{i\eta/2}$ and $p_2 e^{-i\eta/2}$ respectively where p_1 and p_2 are attenuation coefficients along the optic axes and η is the amount of phase retardation. PS images were plotted as accumulative phase retardation with respect to the surface states, and displayed in a gray scale, as black for 0°, and white for 180° phase retardations, and then wrapped back to black for 360°. Diattenuation was quantified by the ratio $d = (p_1^2 - p_2^2)/(p_1^2 + p_2^2)$ where $-1 \leq d \leq 1$ [34].

3. Results

3.1. System verification
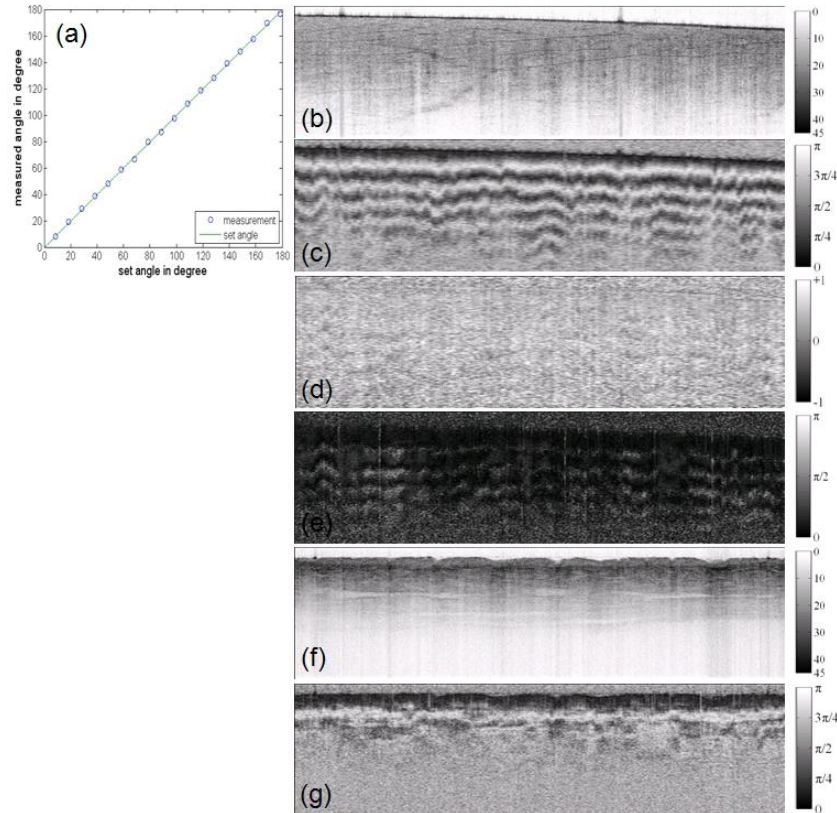
Fig. 2. Verification of PS-OFDI with various test samples. The image size is 8 mm (transversal) x 3.2 mm (axial) in air. (a) a plot of measured optic axis changes vs. set angle changes with a thin polarizer. (b-e) PS-OFDI images of chicken muscle: (b) intensity, (c) accumulated phase retardation, (d) diattenuation, (e) optic axis. (f-g) PS-OFDI images of human skin: (f) intensity, (g) accumulated phase retardation.

The new PS-OFDI system and analysis method were tested by imaging various specimens. First, a thin polarizer was used as a pure diattenuator to verify the PS analysis method. The optic axis and transmission coefficients p_1 and p_2 of the polarizer were measured by imaging its top and bottom surfaces. This measurement was repeated with a stepwise rotation of the polarizer by 10° for every measurement until 180° rotation was reached. The measured optic axis was plotted with respect to the set optic axis (Fig. 2a). Ratio of p_1 to p_2 was typically 1/1000, and the correlation between the set and measured optic axis was 0.994 and the standard deviation was 0.02 degrees. Second, chicken muscle and human skin were imaged as representative birefringent tissues. These samples were imaged by using a custom hand-held probe, which had an optical window slanted by 10° with respect to the propagation direction of the sample beam in order to avoid back reflection from the window surface. During

imaging, the optical window pressed the tissue samples gently, which flattened tissue surfaces.

Chicken muscle was imaged ex-vivo and a human hand was imaged in vivo. Representative images are shown in Fig. 2(b-g). Chicken muscle images show relatively amorphous structures in the intensity image (2b), rapid change of accumulated phase retardation throughout the tissue in the PS image (2c), a relatively uniform diattenuation (2d) and the optic axis orientation (2e). The optic axis image shows a uniform orientation of the optic axis in the top layer, over the first black-white-black phase retardation band in Fig. 2c. Then the optic axis appears to change (transition to white), which repeatedly appears with the depth. This apparent change in the optic axis is attributed to the instability of the optic axis orientation algorithm: when the polarization state reflected at a particular depth is nearly equal to the polarization state reflected at the surface, the optic axis needs to be calculated from the difference of nearly identical states. This occurs when the phase retardation reaches 360°, which is at the first, second third, etc black band in Fig. 2e. Human hand images show the epidermis and dermis of skin in the intensity image (2f) and PS image (2g). The change of accumulated phase retardation occurs in the dermis, which is associated with collagen composition.
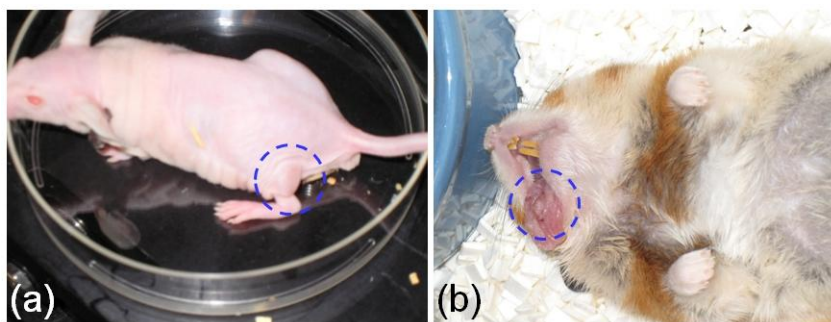
3.2. In vivo animal model imaging

Fig. 3. Picture of animal models imaged by PS-OFDI, (a) mouse cancer model, (b) hamster cheek pouch model

After the verification steps with the test specimens, the new PS-OFDI was applied to imaging two animal cancer models shown in Fig. 3. These were a mouse cancer model by injecting cancer cells subcutaneously, and a hamster cheek pouch model which is a well known oral cancer model [35]. In preparation of the mouse cancer model, a human pancreatic cancer cell line (AsPC-1) was obtained from the American Type Culture Collection (ATCC), and was maintained in a medium recommended by the ATCC at 37°C in a humidified atmosphere of 5% CO2. 6 to 8-week-old male nu+/nu + mice (quantity: 4) were purchased from Cox-7 Animal Facility (Boston, MA). Animal use was approved by the Massachusetts General Hospital IACUC. Mice were subcutaneously injected with AsPC-1 cells (50×10^6/ml) in 100uL Phosphate Buffered Saline solution (VWR) containing 50% matrigel (BD Biosciences) in both legs. Imaging was conducted longitudinally from day 1 until day 10 after injection by using the custom hand-held probe. In preparation of the hamster cheek pouch model, golden Syrian hamsters were purchased from Charles River Laboratories, Wilmington, MA. Pre-malignant and invasive mucosal pouch lesions were induced by application of 0.2ml of 0.5% 9, 10-dimethylbenzanthracene (DMBA) in mineral oil applied 3 x weekly for 10-15 weeks. During DMBA applications the animals were anesthetized with isoflurane by inhalation. PS-OCT imaging was conducted in vivo under anesthesia, by pulling out the lesion in the cheek pouch from the mouth and by using the custom hand-held probe. Out of longitudinal images of mouse cancer models one representative 3D image, which was taken on day 5, is shown in Fig. 4. Intensity image shows the skin on the surface and the muscle/cancer layer below. The muscle layer can be shown in this image, because the mouse skin layer is thin. The skin is

highly scattering with layered structures, and the muscle/cancer layer is less scattering with homogeneous structures. The cancer section appears more scattering than the normal muscle section.
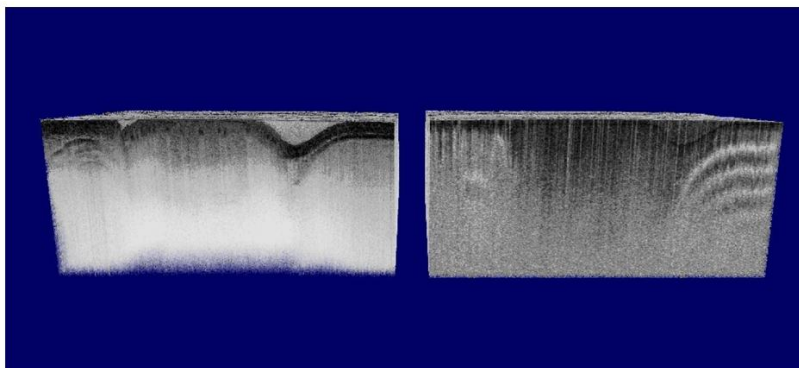

Fig. 4. 3D reconstructed PS-OFDI image of mouse cancer model (Media 1). The imaging size is 12 mm x 12 mm x 3.2 mm in width, length, and depth (in air) respectively with 1000 depth profiles per cross-sectional image.

These two sections are very well distinguishable in the PS image due to the difference in tissue birefringence. The cancer section appears to be separated from the surrounding normal muscle section in both intensity and PS images. This separation was confirmed by histology.

A 3D reconstructed image of the hamster cheek pouch model is shown in Fig. 5. In the intensity image, the cancer and normal cheek pouch tissue sections are not distinguishable, because the tissue surface was deformed by the optical window of the hand-held probe. However, the PS image shows significant contrast between them based on the banding pattern, because the normal cheek pouch tissue is birefringent and the cancer tissue is not. Some banding pattern appears at the bottom of the cancer tissue, and this may indicate the presence of normal tissues below the cancer.
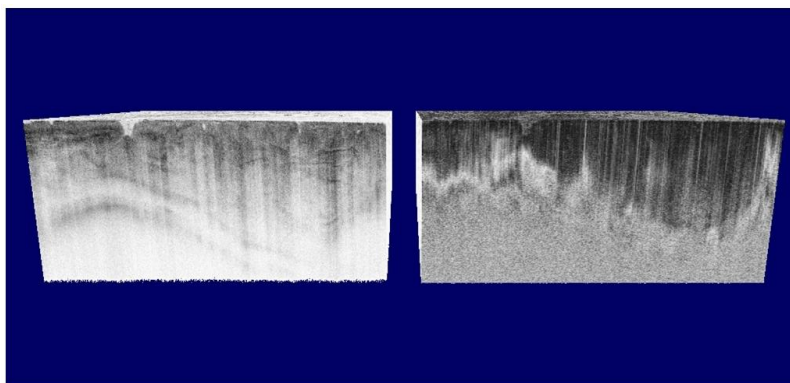
4. Discussion

Fig. 5. 3D reconstructed PS-OFDI image of hamster cheek pouch (Media 2). The image size is same as Fig. 4.

A new PS-OFDI system based on unpolarized light was implemented successfully. Unpolarized light, composed of two uncorrelated polarization states separated by 180° on the Poincaré sphere, probed a sample, and the depth resolved Jones matrix of the sample was constructed by combining the two measurements with different incident polarization states. Because reflection of the two incident polarization states was measured simultaneously, the phase relationship between reflected polarization states was available and the full sample

Jones matrix could be measured and analyzed by eigenvector decomposition. This new method was verified by imaging various control specimens such as a polarizer, chicken muscle, and skin.

Since these Jones matrices contain all the information of polarization properties of the sample, individual parameters can be extracted by an analytical decomposition method [36]. However, a simple eigenvector decomposition method provided better immunity to noise and was used in our PS analysis. A more robust analytical analysis method with better noise immunity may need to be developed to take advantage of the full sample Jones matrices to e.g. determine the optic axis of diattenuation and birefringence independently.

Acknowledgements